PASJ: Publ. Astron. Soc. Japan **56**, 509–519, 2004 June 25

CIAO: Coronagraphic Imager with Adaptive Optics on the Subaru Telescope

Koji MURAKAWA,[1] Hiroshi SUTO,[1] Motohide TAMURA,[2] Norio KAIFU,[2]
Hideki TAKAMI,[1] Naruhisa TAKATO,[1] Shin OYA,[1]
Yutaka HAYANO,[2] Wolfgang GAESSLER,[3] and Yukiko KAMATA[2]
[1]*Subaru Telescope, National Astronomical Observatory of Japan, 650 North A'ohoku Place, Hilo, HI 96720, USA*
murakawa@naoj.org
[2]*National Astoronomical Observatory, 2–21–1 Osawa, Mitaka, Tokyo 181–8588*
[3]*Max-Plank Institute für Astronomie, Königstuhl 17, 69117 Heidelberg, Germany*

(Received 2003 August 12; accepted 2004 March 22)

Abstract

We present the performances of direct imaging with adaptive optics, coronagraph, and imaging-polarimetry of the coronagraphic imager with adaptive optics (CIAO) for the Subaru telescope. Combining with the 36-element adaptive optics system, CIAO produces high-resolution images with a full width at half maximum of 0.″072 and a Strehl ratio of 0.28 in the K band. CIAO has a Lyot's-type stellar coronagraph facility with 0.″1 to 4.″0 diameter masks. The limiting magnitude difference of a companion star at the K band is 11.0 mag at 5σ, 10 minutes integration time, and 2.″0 separation from the central star. CIAO also has a polarimetry facility with a rotatable half-wave plate and a wire grid polarizer. Currently, the measurement of JHK band linear polarization is available.

Key words: instrumentation: coronagraph — instrumentation: polarimetry

1. Introduction

The 8–10 m large telescopes that have been built within the past 15 years have adaptive optics (AO) system. This configuration enables astronomers to break the limitation of image quality by natural seeing and to reach nearly the diffraction-limited image quality at near infrared. The Subaru telescope currently has a 36-element AO system (Usuda et al. 2003; Iye et al. 2004; Takami et al. 2003). While the typical natural seeing limitation at Mauna Kea is 0.″6–0.″7 at the R band, the Subaru telescope with AO produces a sub-0.″1 resolution in the near infrared region. We have considered that a unique near-infrared instrument with a stellar coronagraph and imaging-polarimetry facilities utilizing this high-performance imaging capability. We manufactured a camera, named coronagraphic imager with adaptive optics (CIAO) (Tamura et al. 2000; Murakawa et al. 2003). Our main scientific goals are studies of stars from birth to death. We aim (1) to detect protoplanetary disks and jets around YSOs, (2) to detect companion brown dwarfs and extra-solar planets around nearby stars, (3) to detect debris disks around Vega-like stars, and (4) to image the circumstellar envelope around late type stars. CIAO is also good for detecting circumnuclear regions around AGN and quasar host, and for imaging objects in our solar system.

Stellar coronagraph is a powerful technique for the detection of a faint object around a bright source, and is based on the solar-coronagraph, which was originally invented by Lyot in 1930. Smith and Terrile (1984) successfully imaged a debris disk around a Vega-like star, β-Pic, using a Lyot's-type coronagraph optimized for non-solar objects. While their original experiment used a 7″ occulting mask, the combination of CIAO, AO, and the 8 m Subaru telescope now allows the use of masks with a diameter down to 0.″1. Such a capability enables us to probe regions with a scale of our solar system around stars at 10–100 pc.

Polarimetry is a powerful technique used to investigate the properties of dust in the circumstellar envelope (CSE) around evolved stars and young stellar objects (YSOs). In such an environment, polarization is detected as scattering or absorption by dust particles, and can provide important hints on the dust distribution, size distribution, illumination source, and alignment of dust particles. Considering typical distances of YSOs in nearby molecular clouds or late type stars in our Galaxy of 0.1–1 kpc, an angular resolution of sub-0.″1 corresponds to 10–100 AU scale. We now have a possibility to image regions in which pre-planets form around YSOs and regions in which the most recent mass losing occurs around late type stars.

In section 2, the configuration, characteristics, and basic performances of CIAO will be reported. In section 3, direct imaging with AO is compared with that without AO and image quality, and its properties are summarized. In section 4, the coronagraph point-spread function (PSF) is analyzed and two important coronagraph performances of PSF halo suppression and the limiting magnitude difference of companion are discussed. A coronagraph image of a red supergiant star, VY CMa, is compared with its non-coronagraph imaging to demonstrate the advantage of coronagraph imaging. In section 5, the instrumentation of the polarimetry facility is presented. A result of J-band imaging-polarimetry of a bipolar reflection nebula, OH 0739−14 is demonstrated.

2. Configuration, Characteristics, and Basic Specifications

Figure 1 shows the configuration of the CIAO instrument, the AO system, and the Subaru telescope. The CIAO instrument is equipped in a 2 m × 2 m × 1.7 m container and is

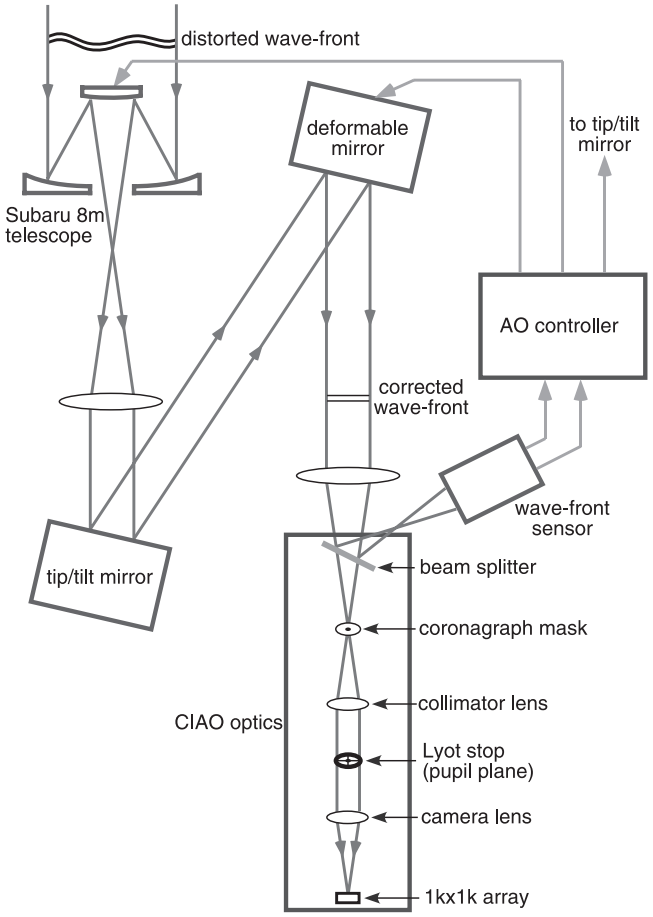

Fig. 1. Schematic of the CIAO instrument. Only a configuration including CIAO, AO, and the Subaru telescope is drawn.

mounted at the Cassegrain focus of the Subaru Telescope. AO optics is installed at a bottom layer of the telescope, and is between the telescope optics and the CIAO optics. The AO system measures the wave-front of star light distorted by the atmosphere with a wave-front sensor and corrects it in real time using a tip/tilt mirror and a deformable mirror. The corrected wave front goes into the CIAO optics. All of the CIAO optical components are positioned in a cooled cryostat.

Light entering the instrument first reaches a beam splitter. It transmits infrared light ($\lambda \geq z$ band) toward the CIAO's science optics and reflects visible light (R band) toward the wave-front sensor. At the Cassegrain focus transferred on the inside of the CIAO optics, a mask wheel is placed. It has 18 positions. Coronagraph masks and a slit for a Wollaston prism are installed in it. These masks are shaped by sputtering of chromium dioxide on a 5 mm thick sapphire substrate. Currently, 12 coronagraph masks with a diameter from $0\farcs1$ to $4\farcs0$ and with 2% transmission are available. The observers can choose the most suitable mask component during an observation. The collimator lens forms an image of the secondary mirror of the telescope at the pupil plane. The collimator lens unit is mounted on a XY stage, and is moved for optical alignment between the telescope optics and the CIAO optics. A stop wheel is placed at the pupil plane. It has 8 positions. Three of them have a cross pattern with a disk at the center to block the secondary supporter pattern and the telescope center hole. These were designed for reducing the diffraction pattern due to such an aperture shape. Another has an off-axis small circular hole whose diameter corresponds to an aperture of a 1.7 m telescope. It gives a symmetric PSF shape. These four components can be rotated while synchronizing with the motion of the instrumental rotator. The other four have a different aperture size, and one of them has a gradient transmission at the pupil edge. There are three filter wheels after that. Each has 10 filter positions with a 1.5 inch diameter. CIAO has $zJHKK_sL'M'$ broad-band filters (astronomical consortium standards), 13 narrow-band filters of Paβ, J continuum, [Fe II], CH_4 on, CH_4 off, H continuum, Brγ, H_2 $v = 1$–0 S(1), H_2 $v = 2$–1 S(1), CO $v = 2$–0, K continuum, H_2O ice, and PAH, a wire grid polarizer, a Wollaston prism, and a neutral-density (ND) filter with 0.7% transmission. CIAO has three camera lens optics. Two are of high-resolution mode (HRM) with 11.5 mas per pixel (FOV $\sim 11\farcs7$) and medium-resolution mode (MRM) with 21.7 mas per pixel (FOV $\sim 22\farcs2$). The MRM optics is useful for general purpose and has Nyquist sampling in the K band. The designed value of the Strehl ratio of the CIAO optics is $> 90\%$ at the JHK bands. The other pupil imaging mode (PIM) is for checking the optical alignment between the CIAO optics and the telescope optics. It is normally used at the beginning of an observation. To make an alignment, the collimator lens unit is moved. This optics is also useful for the diagnosis of other optics, such as a dome flat lamp, a telescope calibration lamp, and AO optics. CIAO has a $1\,\mathrm{k} \times 1\,\mathrm{k}$ Aladdin II InSb detector manufactured by Raytheon (the former Santa Barbara Research Center). The pixel size is $27\mu\mathrm{m} \times 27\mu\mathrm{m}$. The wavelength coverage is 0.9 to 5.5 μm. The detector is cooled at 29 K during operation with a closed-cycle cooler manufactured by Sumitomo Heavy Industries, Inc. The temperature is controlled with a temperature controller manufactured by Lakeshore, Inc. We normally apply a bias level of -300 mV, which gives a quantum well with a non-linearity level of $< 5\%$ around ~ 50000 electrons (~ 7000 ADU). A double-sampling method is followed in data acquisition. This method reads out the array signal twice just after starting and finishing exposure, and the output signal is derived from the difference of these two signals. The minimum exposure time per acquisition is 0.18 s. The typical maximum brightness of a single star with only JHK broad-band filters, which gives about 7000 ADU, is about 6 mag without AO, and about 8 mag with AO. The typical readout noise is 25 electrons (rms, DCS) and the dark level is less than 0.3 electrons s^{-1}. CIAO uses a DSP board computer for controlling the array (Onaka et al. 1998). This computer generates an appropriate clock pattern, depending on the exposure time and the number of coadd, and stores image data during each data acquisition. These data are transferred to the CIAO's local workstation (OBE) by direct memory access (DMA). CIAO's observation support software runs on the OBE. It converts all image data into FITS format, and displays them on a viewer. These data are stored on a hard disc on the OBE, and are archived to the STARS archive system. A typical measured duration time for data archive per frame is about 0.8 s.

The throughput and limiting magnitude have been estimated based on the results of observations of photometric standard

Table 1. Summary of characteristics of CIAO.

Detector	Aladdin II, 1024×1024 InSb array
Wavelength coverage	0.9–5.5μm
Readout noise	25 electrons (rms, DCS)
Dark current	< 0.3 electrons s^{-1}
Camera lens	HRM (11.5 mas pix^{-1}, FOV $\sim 11\farcs7$)
	MRM (21.7 mas pix^{-1}, FOV $\sim 22\farcs2$)
	PIM (for checking optical alignment)
Mask	0.1, 0.2, 0.3, 0.4, 0.5, 0.6, 0.8, 1.0, 1.5, 2.0, 3.0, 4.″0 in diameter
	circular shape with 2% transmission
Stop	2 with circular shape (100% and 90% pupil diameter)
	1 with circular shape and with a gradient transmission
	3 with a cross and a disk at center
	an off-axis small stop
Filter	3 filter wheels
	z, J, H, K, K_s, L', and M'
	[Fe II], CH_4 on, CH_4 off, H cont, H_2 $v = 2$–1 S(1), H_2 $v = 1$–0 S(1), Brγ, K cont, CO $v = 2$–0
	Paβ, J cont, H_2O, PAH, ND (0.7% transmission)
Polarimetry	half wave plate (J, H, K bands, MgF_2)
	wire grid polarizer (J to M' bands)
	Wollaston prism (J to M' bands, MgF_2)
Spectroscopy	J to M, $R \sim 100$–400 with 0.″8–0.″2 width slit
	(This observation mode has not been completed.)
Throughput	$\sim 15\%$ (including all optics of telescope, AO and CIAO)
Limiting magnitude	23.4 mag (J), 22.1 mag (H), 21.9 mag (K), 16.5 mag (L'), 12.7 mag (M'),
	1.″0 diameter aperture, 5σ, 1 hr integration time

stars and the measurement of detector noise. A typical value of the throughput, including the telescope optics, AO optics, and CIAO optics, is $\sim 15\%$ from J to M'. The limiting magnitudes at $JHKL'M'$ are 23.4, 22.1, 21.9, 16.5, and 12.7 mag, respectively at 5σ, 1 hour integration time and 1.″0 aperture. Table 1 summarizes the basic characteristics of CIAO. These are also posted on the official CIAO's web page.[1] Some configuration can be changed. Details should be referred on the web page below.

The details of the optical configuration of the coronagraph and imaging-polarimetry are described in sections 4 and 5, respectively. The current spectroscopy mode is not available due to insufficient engineering observation.

3. Direct Imaging with AO

3.1. FWHM and the Strehl Ratio

In order to the evaluate the image quality of direct imaging with AO, we have obtained PSFs at the JHK bands. The observation was carried out on 2002 February 21. The object was a single bright star, HR 2721, with JHK magnitudes of 4.66, 4.29, and 4.12, respectively. The natural seeing was $\sim 0\farcs7$ in the R band. The elevation during this observation was $\sim 58°$. HRM camera with 11.5 mas pix^{-1} was used. An ND filter was used for avoidance of detector saturation. Total integration time was 80 s. A dark frame was subtracted from all of the target images, and the sky level was subtracted. Dome-flat frames were used for flat fielding. Figure 2 shows the JHK band PSF images. The field of view (FOV) is $4\farcs3 \times 4\farcs3$. At the K band, the central core and the first diffraction ring can be clearly seen. The X-shape feature is due to the secondary mirror-support structure. The magnitude differences of the surface brightness of the PSF at the K band are approximately 2.5, 5.0, 7.5, and 9.3 mag at separations from the center of 0.″2, 0.″5, 1.″0, and 2.″0, respectively.

PSF images without AO have been also obtained for comparing with those with AO and estimating the improvement of the image quality using AO. The observations were carried out on different nights from that with AO because of limited engineering times. The natural seeing was 0.″6 at the R band, and there was no significant difference in the sky condition from that with AO.

The full widths at half maximum (FWHMs) and the Strehl ratios were estimated using the APPHOTO package on the image reduction and analysis facility (IRAF). The Strehl ratio was estimated by the ratio of the ratio of the peak intensity to the total flux of the star PSF to that of the ideal PSF. An aperture of 2.″0 in diameter was applied. The results are listed in table 2. The Rayleigh limits at JHK are 0.″039, 0.″051, and 0.″069, respectively. The FWHMs without AO are 0.″54, 0.″43, and 0.″37 and those with AO are 0.″15, 0.″06, and 0.″072 at JHK bands, respectively. The Strehl ratios without AO are 0.0072, 0.014, and 0.03 and those with AO are 0.0296, 0.103, and 0.283 at the JHK bands, respectively. In the HK bands, the FWHMs with AO are comparable with that of the ideal condition. Table 2 summarizes the basic parameters

[1] ⟨http://SubaruTelescope.org/Observing/Instruments/CIAO/index.html⟩.

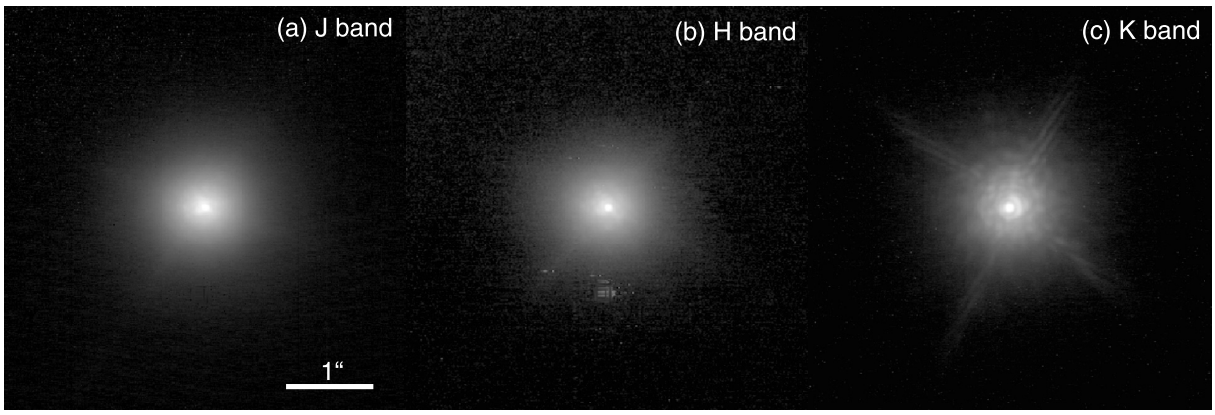

Fig. 2. JHK band images with AO in the logarithmic scale. The scratch patterns below the PSF seen in the H-band image are due to residual bad pixels. The FOV is $4\farcs3 \times 4\farcs3$. The natural seeing was $0\farcs7$ at the R band. The FWHMs and the Strehl ratios in the JHK bands are $0\farcs15$, $0\farcs069$, and $0\farcs072$ and 0.0296, 0.103, and 0.283, respectively. In the K band, the central core and the first diffraction ring are clearly seen. An X-shape artifact and blob-like structures are due to diffraction by the Subaru telescope aperture with the secondary mirror support. These patterns appear more clearly at longer wavelength because the PSF shape reaches a more ideal condition than at a shorter wavelength.

Table 2. FWHMs and the Strehl ratios of PSFs.

	J band	H band	K band
Rayleigh limit	$0\farcs039$	$0\farcs051$	$0\farcs069$
FWHM w/ AO	$0\farcs15$	$0\farcs060$	$0\farcs072$
w/o AO	$0\farcs54$	$0\farcs43$	$0\farcs37$
The Strehl ratio w/ AO	0.0296	0.103	0.283
w/o AO	0.0072	0.014	0.030
Strehl improvement	$\times 4.1$	$\times 7.4$	$\times 9.4$

of the image quality of direct imaging. The Strehl improvement shown in the bottom row of table 2 is defined as the ratio of the Strehl ratio with AO to that without AO. They are 4.1, 7.4, and 9.4 at the JHK bands, respectively.

As can be seen in the Strehl improvement, an AO correction increases the peak intensity by about 10 times. AO compensates the wave-front error at a lower spatial frequency better than that at a higher order. The tip/tilt as the lowest can be corrected the best. The tip/tilt correction fixes the position of the star image on the array. It is understandable that more light energy is collected in the central core of the PSF, and therefore the peak intensity increases compared with that without AO. Without AO, the FWHM at a longer wavelength has a smaller value than that at a shorter wavelength. Since the wave-front error due to atmospheric turbulence at a longer wavelength is smaller, this result is reasonable. On the other hand, those with AO are better in order of the H, K, and J bands, although the Strehl ratios with AO are better in order of the K, H, and J bands. This is because the AO correction in the H band reduces the wave-front error enough to produce a smaller FWHM than that at the Rayleigh limit in the K. If an observation requires a high resolution, H-band imaging would be a good choice. There is another advantage in using the H band rather than in the K band: scattered light by dust in the circumstellar envelope or disk around YSOs or late type stars is larger in H. Therefore, H-band imaging of reflection nebulae often gives a better result than the K band.

3.2. AO Image of a Planetary Nebula, BD +30 3639

We have demonstrated direct imaging with AO of a planetary nebula, BD +30 3639. This object was discovered by Campbell (1893) and is known as “Campbell’s star”. The effective temperature, the distance, and luminosity have been estimated to be ~ 42000 K (Leuenhagen et al. 1996), 1.5 ± 0.4 kpc (Kawamura, Masson 1996), and $L \sim 5.1 \times 10^4\, L_\odot$ (Leuenhagen et al. 1996). This object has a thick ring, extending $3\farcs5 \times 5''$. Extreme mass loss at a rate of $1.3 \times 10^{-5}\, M_\odot\, \mathrm{yr}^{-1}$ is expected to have occurred about 900 years ago. The proper motion of Hα and [N II] line spots was studied, and an expansion velocity of $\sim 30\,\mathrm{km\,s^{-1}}$ was estimated (Li et al. 2002). Waters et al. (1998) found both C-rich and O-rich chemistry in the dust ring. Some emission lines attributed to carbon (e.g. C III λ 5696 and C IV $\lambda\lambda$ 5101/12) were detected (Waters et al. 1998; Grosdidier et al. 2000). In spite of the slow expansion velocity in the ring, a fast wind with a velocity of $\sim 700\,\mathrm{km\,s^{-1}}$ was detected in the central star (Leuenhagen et al. 1996). From such a nature of the central star, there are papers which have classified BD +30 3639 as a [WC9] type Wolf–Rayet star [Acker et al. (1997); Leuenhagen et al. (1996); see also van der Hucht et al. (1981) for characterization of WC-type central stars of planetary nebula].

Figure 3a shows a CIAO + AO image. The observation was carried on 2001 July 8. MRM optics with $21.7\,\mathrm{mas\,pix^{-1}}$ was used. The field of view is $10'' \times 15''$. The light at the K, H, and J bands, is superposed. The FWHMs at JHK are $0\farcs17$, $0\farcs065$, and $0\farcs074$, respectively. Figure 3b shows a composite image at Brγ and H_2 $v = 1$–0 S(1) by Gemini north + Hokupa’a, which is from the public web site issued by Gemini observatory. The Hokupa’a is also a 36-element AO. This configuration is comparable with CIAO and AO. The FWHMs at Brγ and H_2 are $0\farcs077$ and $0\farcs088$, respectively. The CIAO image traces the dust distribution, and clearly resolves the detailed structure of a thick ring and a thin spherical ring with $\sim 3''$ diameter just inside the thick ring. There can be seen small gaps at the north-west and south-east regions. It could be formed by a strong bipolar shock. In the ring, hydrogen is

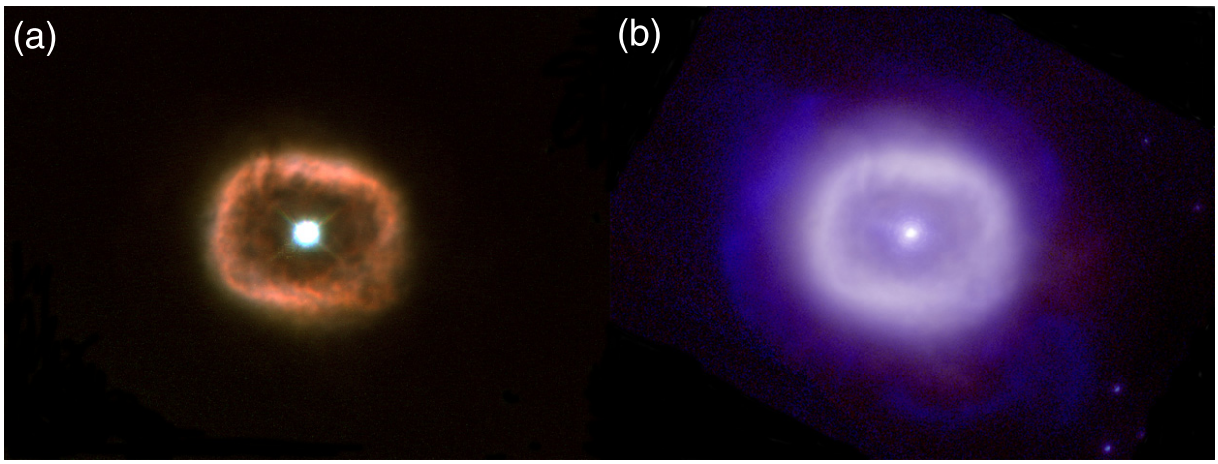

Fig. 3. BD +30 3639 images obtained using CIAO and AO (a) and using Gemini north and Hokupa'a (b). The field of view is $10'' \times 15''$. In the CIAO image, the color composite is made in J, H, and K. A thick ring nebula can be seen. There are gaps at the north east and the south west. In the Gemini image, the color composite is made in Brγ and H_2 $v = 1$–0 S(1).

ionized by strong UV radiation from the central hot star, and Brγ is detected. A faint nebulous feature outside of the ring is an emission line of warm molecular hydrogen in figure 3b.

4. Coronagraph Imaging

CIAO employs a Lyot's-type stellar coronagraph (Lyot 1939). Figure 4 shows the standard configuration, and explains its principle. A occulting mask is placed at the telescope focus. The primary star image that is now intended to be blocked out, should be aligned with the mask center. The intensity distribution after the mask, drawn as a dashed curve, has a disk-like shadow at the center, as shown in the right-top diagram in figure 4. A crown-like intensity distribution forms at the pupil plane due to diffraction by the mask, as shown in right-middle diagram in figure 4. The Lyot stop with a slightly smaller aperture than the pupil (e.g., 90% or 80%) blocks out the high-intensity part at the edge of the pupil. Light from the primary star is therefore effectively attenuated. A comparison of the intensity distribution of the coronagraph PSF of the primary star with that of the non-coronagraph PSF at the array is shown in the right-bottom diagram of figure 4. Light from a companion or nebulous structure outside of the mask forms a disk-like intensity distribution at the pupil, as seen in non-coronagraph imaging. It reaches the array, while losing only a small amount of light energy. As a result, the companion or nebula is detected with a higher contrast than by non-coronagraph imaging.

4.1. Coronagraph PSF and Companion Detectability

We also obtained a coronagraph PSF image on the same night that direct imaging had been done. A $0\farcs2$ diameter mask and a Lyot stop with a 90% pupil diameter were used. The ND filter was removed in the coronagraph observation. The total integration time was 18 s. The same data-reduction procedure was applied. Figure 5a shows a coronagraph PSF image on the logarithmic gray scale. The field of view is $4\farcs3 \times 4\farcs3$. The star image is seen through the mask at the center of the figure. The mask has a transmission of 2%, and is useful for the alignment of a star image through all of the examined frames. Since the exposure time per image acquisition can be extended longer than in non-coronagraph imaging, a cross-shape feature is seen to be stronger than in figure 2.

Figure 5b shows radial profiles of a coronagraph PSF and a non-coronagraph PSF. Both PSF shapes are similar to each other. The average halo suppression in coronagraph imaging is 20%, or 0.24 mag. The result of this low coronagraph performance can be explained as below. The residual wave-front error in the K band after an AO correction still has $1.2\,\mathrm{rad}^2$ which corresponds to a Strehl ratio of ~ 0.3 in the K band. Such a wave-front error smoothes the intensity distribution at the pupil plane. A Lyot stop cannot selectively attenuate light from the central source. Therefore a significant effect is not provided. This is not only a problem in our CIAO, but is a common one among any coronagraph on a ground-based telescope with a non-high order AO.

The companion detectability of the other important coronagraph performance was examined. It is referred to as the limiting magnitude difference of a companion star from the primary star. It is derived from the standard deviation of the surface brightness of the coronagraph PSF through all of the considered frames. The variation of PSF through the frames is often more important than the background noise. This is the most different thing related to the limiting magnitude in standard photometry.

The result is shown in figure 6. The value on the vertical axis is at $5\,\sigma$, and a 10-min integration time. The limiting magnitude differences at $1\farcs0$ and $2\farcs0$ separations are 9.0 and 11.0 mag, respectively. In this result, the noise is dominated by two sources at different separations from the PSF center. Inside of $2\farcs0$, a sufficient number of photons arrive from the star, and the dominant noise is a temporal variation of the PSF shape due to the seeing variation rather than the photon noise. Outside of $2\farcs0$, the read-out noise dominates. This is the reason why the curve in figure 6 drops in a decreasing manner. We must emphasize that this result is just for a typical sky condition, and estimating a limiting magnitude difference for a long integration time is actually difficult, because this performance is very

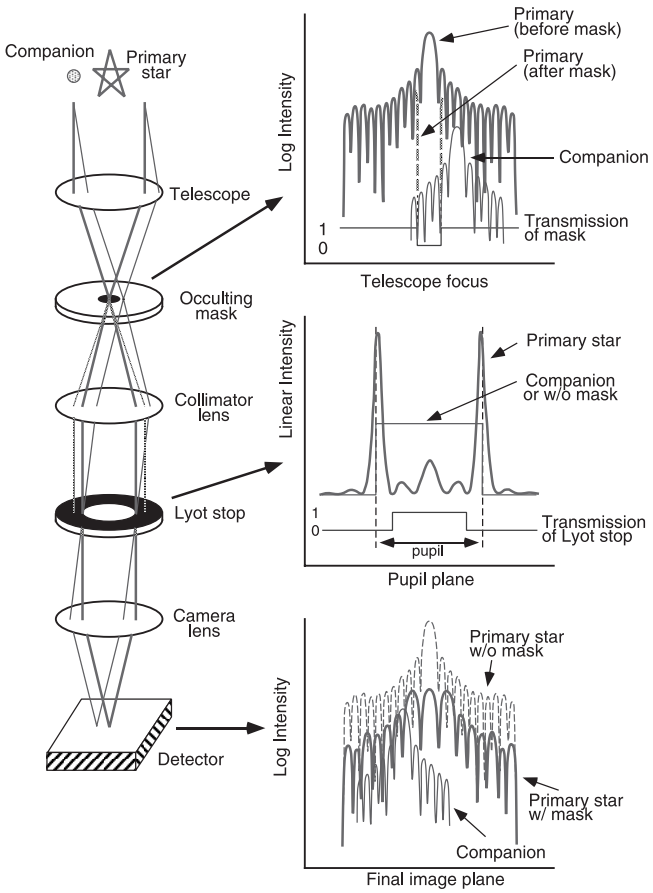

Fig. 4. Standard configuration of the Lyot's-type stellar coronagraph. An occulting mask is placed at the telescope focus to block the primary image. As shown in the right-top diagram, the intensity distribution after the mask has a disk-like shadow at the center of the PSF due to the mask. At the pupil plane, a crown-like intensity distribution forms, as shown in the right middle diagram. The Lyot stop with a slightly smaller aperture than the pupil diameter blocks the major part of the crown-like intensity distribution. The PSF of the primary star is effectively attenuated. The right bottom diagram compares a coronagraph PSF drawn as a thick solid curve and a non-coronagraph PSF drawn as a dashed curve. The light of a companion object or nebula outside of the mask makes a disk-like intensity distribution, and can pass through while losing only a small amount of light energy, similar to the non-coronagraph PSF. As a result, the image contrast of the companion or nebula is expected to have a higher signal-to-noise ratio (SNR) than that of non-coronagraph imaging.

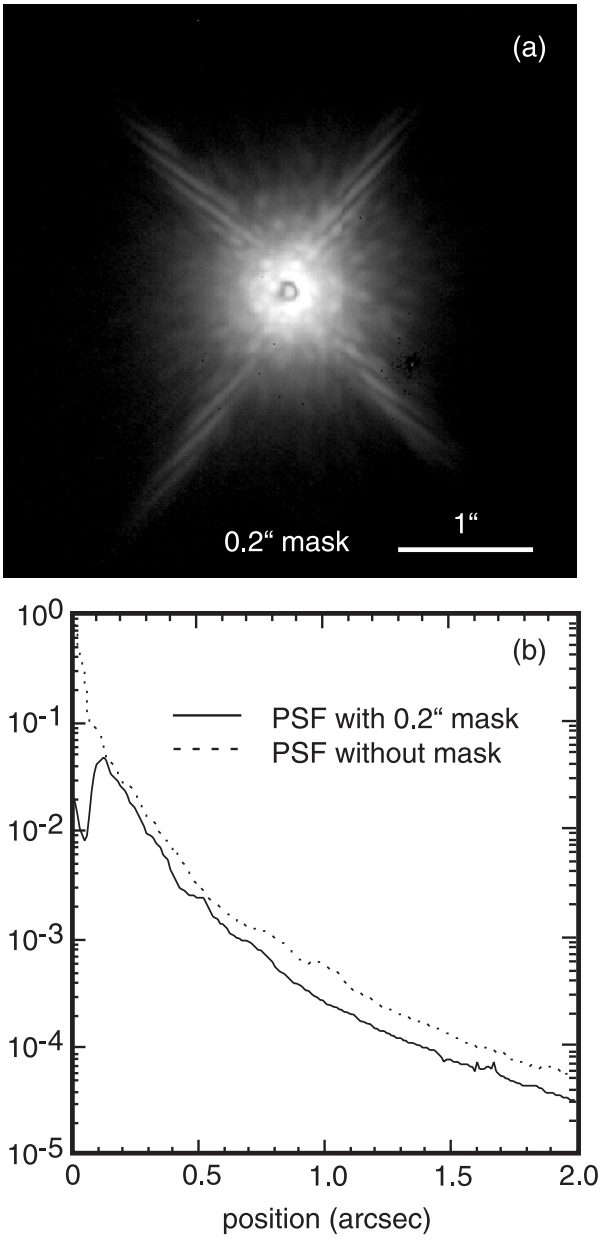

Fig. 5. Coronagraph PSF in the K band (a). A $0\farcs2$ diameter mask is used. The gray level is on the logarithmic scale. The field of view is (a) $4\farcs3 \times 4\farcs3$. A strong X-shape feature is due to diffraction by the secondary supporter. The star image is also seen through a partially transparent mask with a transmission of 2%. A radial profile of the coronagraph PSF inside of $2\farcs0$ is presented with the solid curve in (b). A significant difference in the behavior of the PSF profile inside of $\sim 0\farcs15$ is due to the occulting mask. A PSF without an occulting mask is also drawn with a dotted curve as a comparison in (b). The non-coronagraph PSF was obtained on the same night as that of the coronagraph PSF. The shapes of both profiles appear to be similar to each other. The average PSF halo suppression in the coronagraph PSF is 20%, or 0.24 mag. This result does not sound like that under the ideal condition shown in the right bottom panel of figure 4. Such a limited performance is due to a residual wave-front error, even after an AO correction. This is not a problem in only our CIAO, but also in any other coronagraph on a ground-based telescope. The details are discussed in the text.

sensitive to the seeing condition. It can change during an observation. The seeing size depends on the elevation of the telescope pointing. Observers who try to detect a companion in a critical condition should be careful concerning these points, and should always consider the observation strategy.

4.2. Coronagraph Imaging of a Red Supergiant, VY CMa

In spite of the low-performance of PSF halo suppression described above, there is still an advantage of coronagraph imaging: it reduces the effect of read-out noise. Using VY CMa images shown in figure 7, this is described below.

Figure 7 shows a coronagraphic image and a non-coronagraphic image. MRM camera optics with $21.7\,\mathrm{mas\,pix^{-1}}$

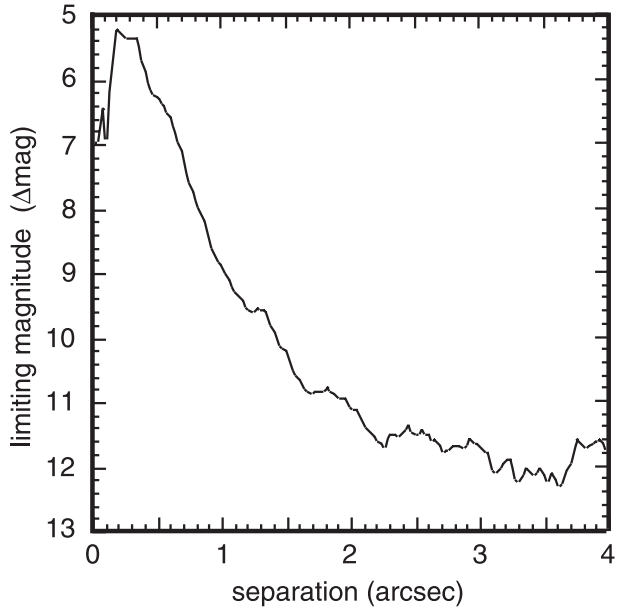

Fig. 6. Limiting magnitude difference of a companion object from the primary. The value in the vertical axis is for that at 5σ, 10-min integration time and the K band. The limiting magnitudes at $1\farcs0$ and $2\farcs0$ are 9.0 and 11.0 mag, respectively. The data is valid at a region with a separation of $\sim 0\farcs4$ or larger because the coronagraph mask exists within this separation. Within $\sim 2''$ from the center, a sufficient number of photons fall, but the SNR is dominated by seeing, rather than the photon noise. Inside of $\sim 2''$, number of electrons to be converted from photons here are comparable with, or less than, that of the read-out noise.

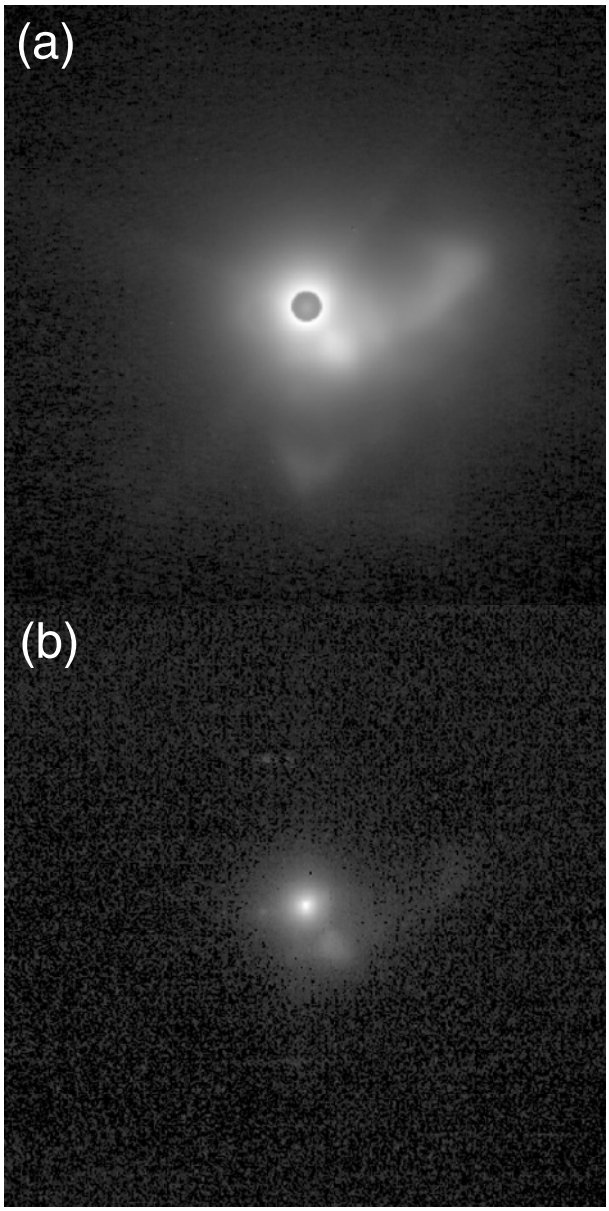

Fig. 7. Coronagraph image with a $0\farcs8$ mask (a) and a non-coronagraph image (b) of VY CMa. The field of view is $17\farcs6 \times 17\farcs6$. The integration times are 120 s and 88 s, respectively. In the coronagraph image, a curved lobe in the west can be seen with sufficient SNR, whereas a poor SNR in a non-coronagraph image. A V-shape feature in the south is detected in only the coronagraph image. Although the wavelengths in (a) and (b) are the J band and H band, respectively, this does not change the discussion.

was used. VY CMa is one of the most luminous red supergiants with $L \sim 4 \times 10^5\, L_\odot$ (Sopka et al. 1985) in the Galaxy. Its distance, spectral type, and luminosity period are ~ 1.5 kpc, M5 Iae, and ~ 2200 d, respectively (Jura, Kleinmann 1990). Its initial mass has been estimated to be 30–40 $M_\odot$, and it is thought to evolve into a Wolf–Rayet star (Meynet et al. 1994). H_2O and OH maser emissions have been detected (Imai et al. 1997; Humphreys et al. 1997; Richards et al. 1998). The H_2O maser sources are distributed in east–west direction, whereas the OH maser sources are in the north–south direction. This would indicate that an equatorial-enhanced disk lies in EW and a polar outflow is in NS. Asymmetric flux distribution is seen in EW in the HST FOC image (Kastner, Weintraub 1998). Monnier et al. (1999) have shown $H\,K\,L$ band images obtained using the Keck I aperture masking technique and J band image using the ESO 3.6 m telescope with ADONIS at La Silla. Dust condensation can be seen with $R \sim 12\, R_*$ as SW, a V-shape structure at the south, and extended nebula up to $4''$. Maihara et al. (1976) have shown a temporal variation in the polarization. Polarization is mainly from reflection nebula by Rayleigh scattering with small grains of radii of $< 0.1\,\mu$m in optical, whereas it is detected in scattering by large grains with radii of $\sim 1\,\mu$m. The peak of polarization had been at $1.6\,\mu$m until 1971. It disappeared in their experiments in 1974 and 1975. This result would suggest a violent and chaotic dust-formation process around VY CMa.

In our experiment, the equivalent integration times were 120 s and 88 s for coronagraph and non-coronagraph images, respectively. In spite of the comparable integration time, the coronagraph image shows nebulosity with sufficient SNR, but worse in the non-coronagraphic image. This is because the exposure time per acquisition can be extended longer in coronagraph imaging than that in non-coronagraph imaging. A larger number of frames should be obtained in non-coronagraph imaging. That causes a larger read-out noise. Consider a rough estimation of this effect. CIAO's coronagraph mask has a transmission of 2%. Coronagraph imaging

allows us to extend the exposure time per image acquisition up to 50 times if we avoid saturation of the detector output level. Non-coronagraph imaging requires 50 more frames than that of coronagraph imaging. The read-out noise is proportional to the square root of the number of frames. As a result, coronagraph imaging can reduce the read-out noise to $\sim 14\%$ $\left(= 1/\sqrt{50}\right)$. The wavelengths in figures 7a and 7b are J and H, respectively, but such a difference does not change this discussion. This kind of advantage is also seen in results of the circumstellar envelope around IRC +10 216 [Murakawa et al. (2002) for coronagraphic images and Murakawa et al. are in preprepreparation of a paper for a non-coronagraphic image].

5. Imaging-Polarimetry

5.1. Instrumentation and Data Reduction

CIAO's polarimetry facility consists of a rotatable half-wave plate (HWP) installed at the Cassegrain focus before both the AO optics and the CIAO instrument and a polarizer installed in a filter wheel in CIAO's cryostat. Only using a polarizer is in principal sufficient for measurement of linear polarization. However, since there are AO optics and CIAO pre-optics of the window, a beam splitter and a compensator that modify the polarization and these optics causes a different polarization efficiency for a different orientation of the polarizer. CIAO's polarimetry facility, therefore, uses a HWP to reduce such instrumental polarization.

The HWP is made of a MgF_2 substrate with a 95 mm diameter, manufactured by Bahnard Hale Co., Ltd. It is an achromat with a wavelength coverage of between 1.0 and 2.5 μm. Currently, JHK band linear polarimetry is available. A wire-grid polarizer was made with aluminum thin wires on a CaF_2 substrate. The calibration data have been obtained on 2003 July 4. The wave retardation of the HWP, $\tau_{\rm HWP}$ was measured in the H band, and the efficiency, $\eta_{\rm HWP} = \cos\tau_{\rm HWP}$ was 0.999. The transmissions of the HWP, $t_{\rm HWP}$, and those of the wire-grid polarizer, $t_{\rm WG}$ and the efficiencies of the wire-grid polarizer, $\eta_{\rm WG}$, at the JHK bands were also measured and are listed in the table 3. The throughput including the HWP and the wire-grid plarizer, $t_{\rm tot}$, and total efficiency, $\eta_{\rm tot}$, are expressed as $t_{\rm tot} = t_{\rm HWP}t_{\rm WG}$ and $\eta_{\rm tot} = \eta_{\rm HWP}\eta_{\rm WG} \sim \eta_{\rm WG}$, respectively. We also used a Wollaston prism made of MgF_2. It splits light into ordinary and extra-ordinary rays, and formed two sets of images on the detector. One of the Stokes QU parameters could be determined at a time. It allowed us to measure the polarization with a higher accuracy than using a wire-grid polarizer. Our Wollaston prism is not currently offered for open-use observations due to a lack of examination of its performance.

Data reduction can follow a standard manner for imaging-polarimetry data. A four-image set with HWP positions of 0°, 45°, 22.°5, and 67.°5 should be required, and that sequence is recommended to be obtained in any observation. The Stokes IQU parameters can be determined from this image set and calibration data described above as $I = (1/2)(I_0 + I_{45} + I_{22.5} + I_{67.5})/t_{\rm tot}$, $Q = (I_0 - I_{45})/(t_{\rm tot}\eta_{\rm tot})$, $U = (I_{22.5} - I_{67.5})/(t_{\rm tot}\eta_{\rm tot})$. The degree of polarization, P, the polarized intensity, PI, and the position angle of the polarization, θ, are derived as $PI = \sqrt{Q^2 + U^2}$ and $\theta = (1/2)\arctan(U/Q)$.

Table 3. Calibration data for polarimetry.

Band	$t_{\rm HWP}$	$t_{\rm WG}$	$t_{\rm tot}$	$\eta_{\rm WG}$
J	0.912	0.425	0.347	0.816
H	0.931	0.432	0.402	0.875
H	0.927	0.461	0.427	0.895

5.2. Imaging-Polarimetry of a Bipolar Reflection Nebula OH 0739−14

OH 0739−14 (OH 238.1+4.2 or IRAS 07399−1435) is a bipolar reflection nebula with a Mira variable, identified as QX Pup in its center. Its evolutionary phase is between an asymptotic giant branch (AGB) and planetary nebula (PN). The luminosity, its period, and the spectral type are $10^4\,L_\odot$ (Kastner et al. 1998), 700 d (Bowers, Morris 1984; Kastner et al. 1992) and M9 III (Cohen 1981; Cohen et al. 1985), respectively. The distance is about 1.5 kpc (Bowers, Morris 1984; Kastner et al. 1992). The detection of OH, H_2O, and SiO masers indicates an oxygen-rich environment in its circumstellar envelope (Morris, Knapp 1976; Engels 1979; Bowers, Morris 1984). Carbon-rich chemistries, such as HCN, CS, and HNC, have also been detected (Deguchi et al. 1979; Morris et al. 1987; Sánchez Contreras et al. 1997). In spite of the detection of C-rich chemistry in the gas phase, a three-micron spectrum predicts the existence of pure water in the solid state (Smith et al. 1988).

We carried out J-band imaging-polarimetry of OH 0739−14 on 2001 December 5. MRM camera optics with 21.7 mas pix^{-1} was used. Since the central star was unseen, and a compact feature at the center of the nebula was extended at a wavelength for wave-front sensing, we did not use AO in this observation. The image quality was limited by the natural seeing, and was 0.″6 in the R band. The integration time was 90 s at a polarization position, and two sets of polarization images were obtained. The total integration time for the total intensity, therefore, was 6 min. Figure 8a shows a total-intensity map on the logarithmic scale. The field of view is $13'' \times 15''$. A bipolar nebula extending in the NNE–SSW direction. The northern lobe shows three lope-like features. The southern lobe has a lope-like feature across the center of the lobe and two major clumps at $(-0.''22, -1.''8)$ and $(-0.''11, -3'')$ from the central clumpy feature. There can also be seen a compact clumpy component between the two lobes. The entire morphology seen in figure 8a is consistent with previous images in the $K_{\rm s}$ band, obtained with SOFI on the ESO 3.5 m NTT telescope (Ageorges, Walsh 2000) and in the K band, obtained with the 4 m telescope on Kit Peak with adaptive optics (Kastner et al. 1998). The resolution is comparable to that of the K band image by Kastner et al. (1998). Figure 8b shows a polarization vector map with log intensity contour lines. The field of view is the same as figure 8a. The polarization vector has been binned 15×15 pixels $(0.''325 \times 0.''325)$ and contour lines are drawn for every 0.5 mag. The polarization vectors show a rough centrosymmetric pattern with its center at the central clumpy feature. The polarizations (P) at the lope-like features in the NS lobes are as large as 30–50%. Such a large polarization and

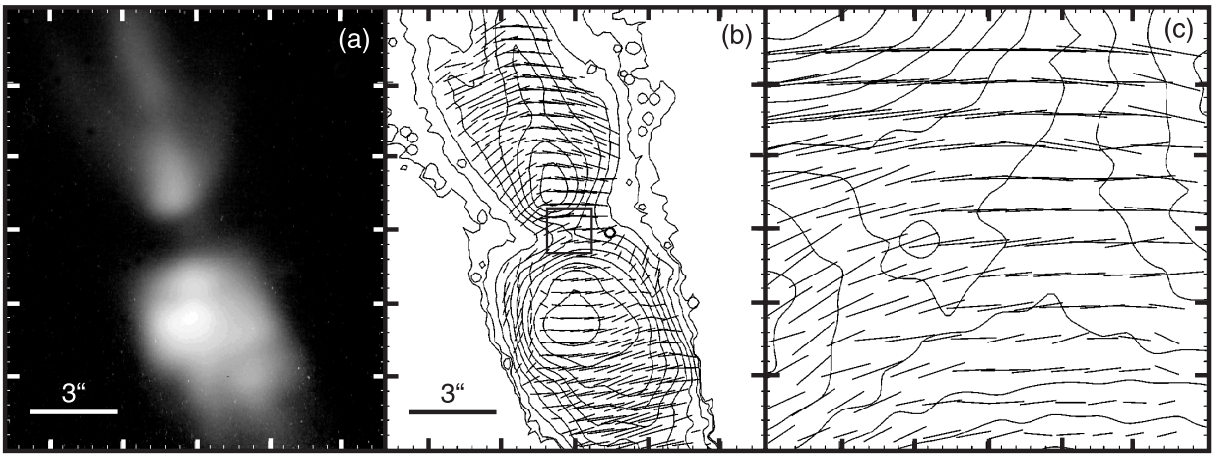

Fig. 8. Total intensity map on the logarithmic scale (a) and polarization vector map with a log-intensity contour map (b) of OH 0739−14. The field of view is $13'' \times 15''$. Contour lines are drawn at every 0.5 mag. The vectors are binned 15×15 pixels ($0\farcs325 \times 0\farcs325$). A bipolar nebula extending NS direction is seen. The large-scale polarization vector shows a rough centrosymmetric pattern surrounding a clump at the center of the bipolar nebula. This polarization vector map shows that the bipolar nebula is seen in the scattering of light from the central star. (c) magnifies the central square box with $1\farcs5 \times 1\farcs5$ region in (b). The contour lines are drawn at every 0.2 mag. The polarization vectors are binned 5×5 pixels ($0\farcs109 \times 0\farcs109$). The polarization vector is aligned perpendicular to the bipolar axis. This is due to the existence of a thick dusty structure, or a dust torus around the central star.

centrosymmetric vector pattern predicts that single scattering with small particles in the structure dominates. Meanwhile the polarization around this features has 10–30%. This difference of polarization might be due to different scattering angle which is resulted by a different geometry. A scattering angle at the lope-like features would be closer to 90° than that around the feature. Figure 8c magnifies a central $1\farcs5 \times 1\farcs5$ region, drawn as a square box in figure 8b. The HST NICMOS images of F205W, F160W, and F110W revealed the central region as an elongated clump (Meakin et al. 2003) with its position angle of the major axis perpendicular to the bipolar axis. The orientation of the polarization vector in this region is mostly aligned parallel to the bipolar axis, and the polarization has 30–40%. Since the central compact clump is resolved in our image, this polarization properties would be characterized by the central dusty structure rather than by a contamination by highly polarized light from the bipolar cavity near the central clump. Such an asymmetric morphology associated with a bipolar structure is often seen in PPNs, and is important in the morphological evolution from the late AGB phase to the PPN phase.

Meixner et al. (1999) and Ueta et al. (2000) have revealed by optical and mid-IR survey observations that a superwind starts to blow at the late AGB phase and must play an important role in shaping the axisymmetric appearance. There are currently two major hypotheses to explain the mechanism of such axisymmetric mass loss, although they are still controversial. One is a companion, and the other is a magnetic force. In the case that a thick dusty torus surrounding the central source, like OH 07139−14, a spectroscopic measurement of the Doppler shift, or a luminosity curve, is powerful to detect a companion. Gómez and Rodríguez (2001) and Sánchez Contreras et al. (2000) have found multi components in the velocity distribution of OH and H_2O masers, and a SiO maser, respectively. Furthermore, the fluxes in the near-IR (Feast et al. 1983) and in 1667 MHz OH maser (Bowers, Morris 1984) vary sinusoidally with a similar period of ~ 650 d. These results support the existence of a companion with a comparable mass with the primary. On the other hand, imaging polarimetry can be a technique for modeling the dust morphology, its distribution in the circumstellar envelope and interaction with the magnetic field. Blackman et al. (2001) have theoretically predicted that a differential rotation of the stellar atmosphere of AGB stars can form a sufficient magnetic field to drive equatorially enhanced mass losing. Greaves (2002) performed imaging polarimetry of a PN, NGC 7027, and a PPN, AFGL 2688 at sub-mm wavelength, and found a linear polarization with its orientation parallel to that of the elongation of the circumstellar envelope. This result would support that such polarization is due to emission by elongated and magnetically aligned dust particles in the circumstellar envelope. Further systematic imaging polarimetry with AO at near-IR of stars with their evolutionary stage from late AGB to PPN and dust modeling of them will provide a better understanding of the precise morphological evolution, and the interaction of dust with the magnetic field.

6. Summary

We have presented the performances of direct imaging with AO, coronagraph imaging, and imaging polarimetry of a near-infrared camera, named CIAO, for the Subaru telescope.

Combined with the current 36-element AO system, CIAO produces high-resolution images with FWHMs of $0\farcs15$, $0\farcs060$, and $0\farcs072$. At the HK bands, the FWHMs are comparable to those in the ideal condition. The Strehl ratios and their improvement compared with PSFs without AO are 0.0296, 0.103, and 0.283, and 4.1, 7.4, and 9.4, respectively. The most significant improvement of PSF with AO is a tip/tilt correction, as the lowest-order wave front error. As a result, the Strehl ratio increases, but the halo component decreases only slightly. As a demonstration of direct imaging with AO, a JHK band composite image of a planetary nebula, BD +30 3639, was

presented. Our image clearly resolved gaps in the ring-like nebula at NE and SW, and revealed a faint thin ring with a 3″ diameter.

Two important performances of coronagraph imaging have been discussed. The PSF halo suppression in coronagraph imaging of CIAO is 20%, or 0.24 mag, at K band, while the ideal condition gives ~ 2.5 mag. Such a large difference is due to a residual wave-front error (cf. the Strehl ratio of ~ 0.3 or $1.2\,\mathrm{rad}^2$). This is a problem in any other ground-based coronagraph with a non-high-order adaptive optics system. The limiting magnitude difference was derived from the variation of the PSF halo component, frame by frame, and was 9.0 and 11.0 mag in the K band, at 1.″0 and 2.″0, respectively, at 5σ SNR and 10-min integration time. Inside of 2″ from the central star, the dominant noise source is a temporal variation of the PSF shape, rather than photon noise, read-out noise or sky-background noise. Outside of 2″, the effect of read-out noise is the major noise source. The advantage of the current coronagraph imaging on CIAO is a reduction of the effect of the read-out noise. A simple analysis predicts that the effect becomes 14% in CIAO's coronagraph. An observational result was demonstrated to show this advantage. A coronagraph image of a red supergiant, VY CMa, was compared with a non-coronagraph image. In spite of comparable integration times, the coronagraph image detects a V-shape feature at 4″ south from the center, and shows a curved lobe extending up to $\sim 4''$ west with a better SNR than the non-coronagraph image.

The instrumentation of the polarimetry facility, its standard observation and data reduction have been presented. It employs a rotatable HWP and a polarizer. A measurement of the linear polarization in the JHK bands has been currently available. A preliminary result of J-band imaging-polarimetry of a PPN OH 0739−14 was presented. A centrosymmetric polarization vector pattern with a high polarization of 10–50% can be seen in the bipolar nebula extending toward NNE–SSW. At the central clump, the polarization vectors are aligned perpendicular to the bipolar axis. This polarization configuration predicts that the clumpy feature has a torus-like dust distribution around the central sources, rather than a simple spherical one. This kind of experiment is important for studying the morphological evolution from the late AGB phase to the PPN phase, in which axisymmetric mass loss begins. Imaging-polarimetry is a useful technique for dust modeling, and can provide a better understanding of a mechanism to form such an axisymmetric appearance.

We would like to thank the Subaru telescope group, both in Hawaii and Mitaka, for their support and encouragement. In particular, we wish to give special thanks to Dr. M. Tanaka for useful discussions and comments through out the whole text. We also thank Dr. T.-S. Pyo for discussions concerning the physics of the circumstellar envelope, Dr. J. Morino for discussions about coronagraph imaging, Dr. A. Tajitsu and Dr. T. Ueta for discussions about BD +30 3639, and Mr. B. Holms, Mr. L. Ramos, and Mr. Y. Doi for providing much technical support.

References

Acker, A., Grosdidier, Y., & Durand, S. 1997, A&A, 317, L51
Ageorges, N., & Walsh, J. R. 2000, A&A, 357, 661
Blackman, E. G., Frank, A., Markiel, J. A., Thomas, J. H., & van Horn, H. M. 2001, Nature, 409, 485
Bowers, P. F., & Morris, M. 1984, ApJ, 276, 646
Campbell, W. W. 1893, PASP, 5, 204
Cohen, M. 1981, PASP, 93, 288
Cohen, M., Dopita, M. A., Schwartz, R. D., & Tielens, A. G. G. M. 1985, ApJ, 297, 702
Deguchi, S., Claussen, M. J., & Goldsmith, P. F. 1986, ApJ, 303, 810
Engels, D. 1979, A&AS, 36, 337
Feast, M. W., Catchpole, R. M., Whitelock, P. A., Roberts, G., Jones, J. S., & Carter, B. S. 1983, MNRAS, 203, 1207
Gómez, Y., & Rodríguez, L. F. 2001, ApJ, 557, L109
Greaves, J. S. 2002, A&A, 392, L1
Grosdidier, Y., Acker, A., & Moffat, A. F. J. 2000, A&A, 364, 597
Humphreys, R. M., et al. 1997, AJ, 114, 2778
Imai, H., et al. 1997, A&A, 319, 1
Iye, M., et al. 2004, PASJ, 56, 381
Jura, M., & Kleinmann, S. G. 1990, ApJS, 73, 769
Kastner, J. H., & Weintraub, D. A. 1998, AJ, 115, 1592
Kastner, J. H., Weintraub, D. A., Merrill, K. M., & Gatley, I. 1998, AJ, 116, 1412
Kastner, J. H., Weintraub, D. A., Zuckerman, B., Becklin, E. E., McLean, I., & Gatley, I. 1992, ApJ, 398, 552
Kawamura, J., & Masson, C. 1996, ApJ, 461, 282
Leuenhagen, U., Hamann, W.-R., & Jeffrey, C. S. 1996, A&A, 312, 167
Li, J., Harrington, J. P., & Borkowski, K. J. 2002, AJ, 123, 2676
Lyot, B. 1939, MNRAS, 99, 580
Maihara, T., Noguchi, K., Oishi, M., Okuda, H., & Sato, S. 1976, Nature, 259, 465
Meakin, C. A., Bieging, J. H., Latter, W. B., Hora, J. L., & Tielens, A. G. G. M. 2003, ApJ, 585, 482
Meixner, M., et al. 1999, ApJS, 122, 221
Meynet, G., Maeder, A., Schaller, G., Schaerer, D., & Charbonnel, C. 1994, A&AS, 103, 97
Monnier, J. D., Tuthill, P. G., Lopez, B., Cruzalebes, P., Danchi, W. C., & Haniff, C. A. 1999, ApJ, 512, 351
Morris, M., Guilloteau, S., Lucas, R., & Omont, A. 1987, ApJ, 321, 888
Morris, M., & Knapp, G. R. 1976, ApJ, 204, 415
Murakawa, K., et al. 2002, A&A, 395, L9
Murakawa, K., et al. 2003, Proc. SPIE, 4841, 881
Onaka, P. M., Tokunaga, A. T., Kobayashi, N., Weber, M., Rayner, J. T., Denault, A. J., Watanabe, D. Y., & Ching, G. K. 1998, Proc. SPIE, 3354, 30
Richards, A. M. S., Yates, J. A., & Cohen, R. J. 1998, MNRAS, 299, 319
Sánchez Contreras, C., Bujarrabal, V., & Alcolea, J. 1997, A&A, 327, 689
Sánchez Contreras, C., Bujarrabal, V., Miranda, L. F., & Fernández-Figueroa, M. J. 2000, A&A, 355, 1103
Smith, B. A., & Terrile, R. J. 1984, Science, 226, 1421
Smith, R. G., Sellgren, K., & Tokunaga, A. T. 1988, ApJ, 334, 209
Sopka, R. J., Hildebrand, R., Jaffe, D. T., Gatley, I., Roellig, T., Werner, M., Jura, M., & Zuckerman, B. 1985, ApJ, 294, 242
Takami, H., Takato, N., Hayano, Y., Iye, M., Kamata, Y., Minowa, Y., Kanzawa, T., & Gaessler, W. 2003, Proc. SPIE, 4839, 21
Tamura, M., et al. 2000, Proc. SPIE, 4008, 1153

Ueta, T., Meixner, M., & Bobrowsky, M. 2000, ApJ, 528, 861
Usuda, T., et al. 2003, Proc. SPIE, 4837, 831
van der Hucht, K. A., Conti, P. S., Lundstrøm, I., & Stenholm, B. 1981, Space Sci. Rev., 28, 227
Waters, L. B. F. M., et al. 1998, A&A, 331, L61